Quantifying Sub-Meter Surface Heterogeneity on Mars Using Off-Axis Thermal Emission Imaging System (THEMIS) Data

B.E. McKeeby[1], M.S. Ramsey[1], C.J. Tai Udovicic[2], C. Haberle[2], C.S. Edwards[2]

[1] Department of Geology and Environmental Science, University of Pittsburgh, Pittsburgh, PA, USA

[2] Department of Astronomy and Planetary Science, Northern Arizona University, Flagstaff, AZ, USA

Corresponding author: B.E. McKeeby (bem101@.pitt.edu)

Department of Geology and Environmental Science, 4107 O'Hara St, Pittsburgh, PA 15260

Key Points:

- Using Routine Off-nadir Targeted Observations (ROTOs) of Mars Odyssey we acquire directional thermal infrared spectra of the surface
- Thermal infrared spectral slopes from the ROTO data enable extraction of sub-pixel anisothermal heterogeneities at fine spatial scales
- A thermal inertia mixing model is used to quantify sub-pixel temperature mixing produced by a checkerboard mixing of surface units

Abstract

Surface heterogeneities below the spatial resolution of thermal infrared (TIR) instruments result in anisothermality and produce emissivity spectra with negative slopes at longer wavelengths. Sloped spectra arise from an incorrect assumption of either a uniform surface temperature or a maximum emissivity during the temperature-emissivity separation of radiance data. Surface roughness and lateral mixing of differing sub-pixel surface units result in spectral slopes that are distinct, with magnitudes proportional to the degree of temperature mixing. Routine Off-nadir Targeted Observations (ROTO) of the Thermal Emission Imaging Spectrometer (THEMIS) are used here for the first time to investigate anisothermality below the spatial resolution of THEMIS. The southern flank of Apollinaris Mons and regions within the Medusae Fossae Formation are studied using THEMIS ROTO data acquired just after local sunset. At higher emission angles, differing relative proportions of rocky and unconsolidated surface units are observed. This produces a range of sloped TIR emission spectra dependent on the magnitude of temperature differences within a THEMIS pixel. Spectral slopes and wavelength-dependent brightness temperature differences are forward-modeled for a series of two-component surfaces of varying thermal inertia values. This creates a thermophysical model suggesting a local rock abundance 6 times greater than currently published results and four orders of magnitude more sensitive than those relying on nadir data High-resolution visible images of these regions indicate a mixture of surface units from boulders to dunes, providing credence to the model.

Plain Language Summary

Orbital thermal infrared (TIR) spectral and temperature data are used to determine numerous planetary surface properties, providing insight into how the planet's surface has

evolved. This paper applies a new methodology to examine temperature mixing of surfaces with different units and particle sizes (i.e., rock and dust). Using the Thermal Emission Imaging Spectrometer (THEMIS) TIR data at 100m/pixel we model the emissivity spectra and temperature to derive the abundance of these different surface units. TIR spectra are sensitive to sub-pixel temperature differences at small scales. Surfaces with different components heat and cool at differing rates creating temperature differences within each pixel. The extracted TIR spectra will have a negative slope proportional to the degree of the temperature differences. Using a series of post-sunset TIR images from different viewing angles. We model the surface temperature and spectral slope to derive the percent of surface units present. Matching these results to our observations, allows determination of particle size and abundance of each component. Additionally, this method creates a thermophysical model four orders of magnitude more sensitive than rock abundance models derived from TES thermal inertia. This is critical for understanding modern surface evolution, and for future exploration such as landing site selection.

1. Introduction:

Thermal infrared (TIR) observations of Mars by the multispectral Thermal Emission Imaging System (THEMIS) have been used to determine a wide array of surface and atmospheric properties including surface mineralogy, rock abundance, and thermophysical units, as well as atmospheric dust and water ice contents (Smith et al., 2003; Christensen et al., 2004; Bandfield et al., 2004; Fergason et al., 2006a; Bandfield and Edwards, 2008; Bandfield, 2009; Ahern et al., 2021). Accurate determination of these properties is fundamental to understanding the planet's past and current surface evolution. For example, the correct retrieval of the temperature-independent spectral property of emissivity is key to determining surface

mineralogy and composition (Bandfield et al., 2004). However, this requires the removal of temperature-mixing effects, which can impart unwanted spectral slopes. Commonly, this requires an assumption of an isothermal pixel-integrated surface temperature within the instrument's instantaneous field of view (IFOV). However, if that corresponding area on the ground contains a surface with roughness elements or units with differing thermal inertias (TI), the assumption of a uniform surface temperature becomes invalid, producing an artificial spectral slope.

This work combines a novel off-nadir THEMIS IR dataset, collected by way of Routine Off-nadir Targeted Observations (ROTO) of the Mars Odyssey Spacecraft, with the KRC thermophysical model (Kieffer, 2013) to describe sub-pixel surface units found in the Apollinaris Mons region. Using KRC, we forward model the effects of anisothermality by way of a two-component surface model using units of differing thermal inertias. TIR spectra are sensitive to the degree to which a surface unit remains thermally isolated. This scale is estimated based on the surface's derived thermal inertia (Banfield and Edwards, 2008).

We propose that, due to their unique viewing geometries, ROTOs allow for a more accurate determination of sub-pixel thermophysical properties than traditional methods, especially in regions heavily mantled by dust. For example, in dusty environments, the high emission angles achieved by ROTOs permit the THEMIS IFOV to observe the less dusty sides of rocks whereas nadir observations would only observe the dust mantled tops. The difference in temperature between low thermal inertia dust and high thermal inertia rock produces sub-pixel anisothermality that, if successfully modeled, can be used to derive a local rock abundance model. Determining the grain size is possible where differences in derived TI values result in temperature separability. The work presented here explores derived TI values ranging from 50 to

2500 thermal inertia units (TIU), corresponding to grain sizes ranging from dust to bedrock, respectively

2. Background:

2.1. Thermal Inertia:

Thermal inertia describes an object's response to temperature change, by way of storing and losing heat, and is controlled by the physical properties of the material. Expressed in J m^{-2} K^{-1} $s^{-1/2}$ or TIU, it is defined as the square root of the product of conductivity (k), density (ρ), and specific heat capacity (c). TI is solely dependent on the material itself and is not affected by the latitude, local time, or season. Derived from TIR observations combined with thermophysical models, (Kieffer, 2013; Mellon et al., 2000; Bandfield et al., 2012) TI is extensively used to investigate the surface properties of several planetary bodies, including Mars, the Moon, Mercury, and Phobos (Chase et al. 1976; N. M. Smith et al., 1981; Fergason and Christensen, 2006; Christensen and Kieffer; 2006; Putzig and Mellon; 2007; Edwards et al., 2018; Ahern et al., 2021). However, interpretation of TI can prove complicated due to the complexity arising from various mixing scenarios (homogenous surface, checkerboard mixing, and vertical layering). Additionally, as seen from in-situ surface investigations, more than one material is commonly exposed at the surface (Nowicki and Christensen, 2007). A material's diurnal temperature curve is commonly asymmetrical as its temperature tends to peak in the early afternoon and dissipate during the night. However, if that curve represents mixtures of different TI units, the shape and amplitude of the curve are impacted depending on the relative proportions of those units, their vertical or lateral mixing, and their individual thermophysical properties (Nowiki and Christensen, 2007; Ahern et al., 2021). Separability of mixed component surfaces

with different TI values is possible using TIR spectral data, but only if the temperature contrast between the units is large (Cowart and Rogers, 2021). Here we employ a series of THEMIS ROTO images captured just after sunset and attribute the observed anisothermal spectra to the mixing of surface units with differing TI values.

2.2 Thermal Mixing and Emissivity:

TIR spectra are sensitive to thermal mixing on a broad range of scales including those at or below the spatial resolution of current orbital instruments. The thermal inertia, albedo, and roughness at scales from micrometers to centimeters, combined with the incident solar radiation, determine the kinetic temperature of the surface, independent of its composition. However, the derived pixel-integrated brightness temperature varies as a function of wavelength and degree of sub-pixel temperature mixing. For example, the viewing geometry combined with a mixed temperature surface will result in a different pixel-integrated temperature compared to that from the same surface viewed at nadir (Bandfield et al., 2015). Surfaces containing sub-pixel mixtures of materials of differing thermal inertias typically show variable (anisothermal) surface temperatures as the combined radiance from objects of different temperature no longer match a single blackbody radiance spectrum (Jakosky, 1978; Nowicki and Christensen, 2007; Ahern et al., 2021; Cowart and Rogers, 2021). Here we refer to this as sub-pixel anisothermality.

Changes in the measured emitted radiance from varying emission angles can therefore accentuate this sub-pixel anisothermality, as opposed to other potential causes such as an incorrect assumption of the maximum emissivity (e.g., Bandfield and Edwards, 2008; Osterloo et al., 2008; Bandfield et al., 2015). For example, although nearly all silicate phases exhibit near-unit emissivity at some point in the THEMIS wavelength range, some chloride salts have emissivity values much less than 1.0 (Lane and Christensen, 1998; Osterloo et al., 2008). Where

this occurs and an assumption of 1.0 is used to separate the temperature and emissivity, the target temperature is underestimated and a negatively sloped emission spectrum results (Ruff et al., 1997; Osterloo et al., 2008; Bandfield, 2009). However, variations in viewing geometry or observing conditions of these "graybody" surfaces do not change the magnitude of spectral slopes. Unlike an anisothermal surface where the spectral slope variability is a function of temperature mixing at a particular viewing geometry (Bandfield, 2009).

Where sub-pixel anisothermality occurs within an instrument's field of view, the surface no longer behaves in a Planck-like manner with respect to wavelength and temperature. Instead, the Planck radiance function can only match the measured radiance at a single wavelength. Standard temperature/emissivity separation analysis is therefore flawed, as it relies on the assumption of a homogenous pixel temperature. This results in an emission spectrum with negatively trending slopes at longer wavelengths that may complicate subsequent compositional analysis (Bandfield, 2009; Rose et al., 2014; Bandfield et al., 2015). Our work utilizes specialized instrument pointing angles acquired close in time to maximize off-nadir viewing. At off-nadir emission angles, surface anisothermality varies as different surface units are observed at differing relative proportions. Comparable results are obtained by examining nadir TIR emission spectra collected at varying seasons and local solar times that produce differing solar illumination conditions (Bandfield and Edwards, 2008; Bandfield 2009). However, this alternative method comes with the added complication of surface and atmospheric changes that may occur between nadir observations.

Due to the sensitivity of the TIR spectrum to thermal mixing below the pixel scale, directional emission measurements provide a unique way to retrieve thermophysical properties (Bandfield and Edwards, 2008). The sub-pixel anisothermal effects on the TIR spectrum are

directly proportional to the degree and distribution of macro-scale roughness, and/or the relative proportions of different surface units in each pixel. For example, surfaces with greater degrees of sub-pixel anisothermality exhibit a greater magnitude of negative spectral slopes compared to more isothermal surfaces (Bandfield and Edwards, 2008; Bandfield, 2009; Bandfield et al., 2015; McKeeby and Ramsey, 2020; McKeeby and Ramsey, 2021).

2.3. Thermal Mixing and Brightness Temperature:

Depending on the season, time of day, and latitudinal location of the target, the surface will be colder than the atmosphere. Where this occurs, atmospheric emission is greater relative to surface emission (Cowart and Rogers; 2021). This limits the usability of emissivity over the full THEMIS spectral range due to the inability to perform a complete radiance correction (Bandfield et al., 2004). This is the case with much of the recent THEMIS data acquisitions, which are collected at or near local sunset due to the current Odyssey orbit. In lieu of emissivity, pixel-integrated brightness temperature (BT), derived at wavelengths least affected by the atmosphere, can be used as a proxy to assess the degree of surface thermal mixing. Like emissivity, BT is controlled by surface roughness, local true solar times (LTST), solar longitude (Ls), thermal inertia, and albedo. Additionally, it assumes a wavelength-dependent Planck-like emission and therefore has a negative slope for anisothermality surfaces for the same reasons as the sloped emissivity spectra.

TIR data are sensitive to the scale at which the facets of surface units remain thermally isolated and is estimated based on the surface's TI. At low TI (<100 TIU), the TIR spectrum is sensitive to features on a scale of ~ 1 cm. At a moderate TI (150-300 TIU) this scale increases to ~10 cm and at high TI (>800 TIU) the scale is ~1 m (Bandfield and Edwards, 2008). This is most prevalent during daytime observations where surfaces undergo solar heating. Nighttime thermal

emission measurements on the other hand provide qualitative information on relative differences in surface grain size, degrees of inundation, and total rock abundance (Kieffer et al., 1977; Christenson, 1986; Fergason et al., 2006, Ahern et al., 2021). After sunset, with solar forcing removed, surface units thermally equilibrate at a rate directly proportional to their TI, if thermal diffusion allows anisothermality to exist in the first place. The surfaces studied here have bulk TI values between 300-350 J m^{-2} K^{-1} $s^{-1/2}$ constraining sensitivity to temperature mixing at the ~10 cm scale, three times smaller than HiRISE data and a scale previously only accessible by in-situ investigation.

2.4. ROTO description:

Historically, Routine Off-nadir Targeted Observations (ROTO) by the Mars Odyssey spacecraft have been used to provide off-nadir viewing of the Martian surface since the second extended mission. This has assisted in TIR data acquisition of hard to image targets i.e., polar regions, as well as studies into atmospheric properties using limb measurements and imaging of the Martian moons, Phobos and Deimos (Edwards et al., 2019). Where applied to surface investigations, ROTO data provide a unique view and measure of TIR radiance at varying emission angles within a relatively short acquisition window. For thermophysical studies, ROTO data are typically collected over 2 weeks allowing near-identical surface footprints to be imaged at differing emission angles and under similar LTST, Ls, and atmospheric conditions. This provides an excellent opportunity for the analysis and modeling of anisothermal spectral effects. The first ROTO sequence designed specifically to investigate surface roughness was performed in September 2017 and covered a region within Daedalia Planum centered at 237.62°E and -23.26°N. This area contains a unique set of lava flows that display atypical THEMIS

thermophysical properties recorded during daytime and nighttime overpasses (Crown and Ramsey, 2017; Simurda et al., 2019).

2.5. Study Location:

Apollinaris Mons is a volcanic edifice located between the northern lowland and southern highlands. It covers an area ~190 km wide and features a large summit caldera and a 140 km fan deposit that extends to the southeast (Chuang et al., 2019). A series of eight new ROTO observations were collected from 18:00h to 19:00h LTST, 38° to 47° L_s, 93° to 102° solar incidence, and surface emission angles from -31° to +33° (Table 1). Images are centered around 174.26° E, -6.40°N and cover an area that includes Apollinaris Mons caldera, extends north into the lower Medusae Fossae formation and south towards Gusev Crater (Figure 1). This ROTO campaign was specifically designed to investigate surface thermophysical properties and was chosen due to the documented presence of rough surfaces found in proximity to Apollinaris Mons (Bandfield, 2009; Zimbelman et al., 2010) as well as the contested formation hypothesis of the Medusae Fossae Formation (MFF; Tanaka, 2000; Bradley et al., 2002; Hynek et al., 2003; Mandt et al., 2008).

We selected two study areas within the THEMIS ROTO data that exhibit relatively warm pixels. In-depth spectral and thermophysical analysis was performed to quantify and model the degree of subpixel thermal mixing due to variable surface units. Study area 1 is best described as a warm slope associated with a collapse feature in the Medusae Fossae formation, just north of the Apollinaris Mons complex (Figure 2). This area was chosen because it retains surface temperatures above the atmospheric temperatures for the entire ROTO observational period, allowing us to apply the surface emissivity analysis (Figure 3).

Study area 2 is located at the southwestern edge of the Apollinaris Mons fan deposit before it meets the chaos terrain (figure 2). This unit falls within the fan deposit south of the Apollinaris Mons caldera and is described as rolling plains dominated by volcanic material overlain with aeolian deposits (Scott and West, 1978; Tanaka et al., 2014). The fan deposit covers much of Apollinaris Mons' south flank with a runout distance of ~150km and emanates from a ~2 km wide channel in the caldera rim. The fan is dissected by numerous channels that have been interpreted as bisected by pyroclastic flows, lahars, or other fluvial processes (Gulick and Baker, 1990; Farrell and Lang, 2010; Gregg and Krysak, 2011; Maarry et al., 2012). Impact craters in the fan deposit display a layered texture on their walls with some exhibiting rampart ejecta indicating a volatile-rich substrate at the time of impact (Lang et al., 2010; Maarry et al., 2012).

Due to the season, overpass time, and thermal inertia (TI), much of this surface has brightness temperatures below 200K. These temperatures generally fall below that of the atmospheric temperature at this time of day, requiring the use of brightness temperature analysis for this site. Area 2 lacks the large-scale topographic slopes seen in study area 1 but displays apparent brightness temperatures warmer than the surrounding terrain (Figure 4).

3. Methodology:

3.1 THEMIS instrument and ROTO data description:

THEMIS uses an uncooled microbolometer array with nine spectral channels between 6.8 and 14.9 μm to acquire TIR data at a spatial resolution of ~ 100m/pixel (Christensen et al., 2004). A detailed description of the radiometric calibration and associated uncertainties can be found in Christensen et al. (2004) and Bandfield et al. (2004). The standard THEMIS “4-panel” decorrelation stretch (DCS) image (e.g., Gillespie et al., 1986) sets were used to identify regions

where dominant spectral slopes are present. These images use THEMIS calibrated spectral radiance displayed in 3 separate DCS images and a corresponding surface temperature image (e.g., Bandfield, 2006; 2008; 2009). Here, pixels with anisothermal spectra appear as blue or cyan pixels indicating a negative spectral slope (Figure 2).

Where possible, atmospherically corrected surface emissivity spectra are obtained using the methods described in Bandfield et al. (2004), which assumes an invariant atmosphere over the scene. This provides a straightforward approach to removing atmospheric emission and scattering by first choosing a region of variable temperature but uniform composition within the THEMIS scene. Previously acquired, higher spectral resolution Thermal Emission Spectrometer (TES) data of this region are used to determine the surface emissivity and atmospheric attenuation. The TES-derived atmospheric properties are then removed from the THEMIS data on a pixel-by-pixel basis resulting in atmospherically corrected THEMIS surface emissivity data (Smith et al. 2000; Bandfield and Smith 2003; Bandfield et al., 2004; Bandfield, 2008). However, this approach is only valid where the surface temperatures exceed atmospheric temperature.

Since 2014, the Mars Odyssey orbiter has followed the terminator, allowing for dusk and dawn observations. Although this provides for unique viewing conditions that can accentuate topographic features by illumination at high solar angles, it has created thermal challenges where attempting to accurately measure the surface contribution to the measured radiance. In cases where the atmospheric temperature is greater than the surface temperature, atmospheric emission dominates the radiance spectrum effectively masking surface emission over most of the THEMIS wavelength region. Temperature differences on the surface under these atmospheric conditions can be inferred by examining the brightness temperature differences between wavelengths where

the atmospheric emission is minimal. For this study, brightness temperature differences between THEMIS bands 3 and 9 and from opposing ROTO angles are used.

Brightness temperature is calculated by fitting a plank curve to channels 3 and 9, wavelength-dependent brightness temperatures are then averaged for each. Band 3 was chosen because the atmosphere is relatively transparent at this wavelength and the surface emissivity of most rock-forming minerals is near unity. However, band 3 can be noticeably impacted by dust and water ice in the atmosphere (Smith et al., 2003). Band 9 was chosen as it contains the highest signal to noise and is also relatively transparent to atmospheric dust. However, the wings of the atmospheric CO_2 absorption band may be detected at colder surface temperatures. Band 9 brightness temperatures are calibrated to a precision of 1.2 K and absolute accuracy of 2.8 K at night (Fergason et al., 2006a). To accurately predict the effects of sub-pixel heterogeneity on the measured brightness temperature or emissivity, a model forecasting both realistic temperatures is required (Bandfield and Edwards, 2008; Bandfield, 2009).

3.4 Modeling Approach:

This study utilizes wavelength and viewing angle dependent differences in emissivity or brightness temperature to separate thermally mixed surface units. To achieve this, we forward model the TIR spectral slopes or band-dependent differences in brightness temperature using a two-component thermal model. In doing so, we create a rock abundance model that accounts for off-nadir THEMIS viewing geometries and is four times more sensitive than those relying upon THEMIS nadir derived thermal inertia. We utilize the KRC model (Kieffer, 2013) to predict surface temperatures for a range of thermal inertia values at each THEMIS observation used in this study. Model inputs accounted for latitude, longitude, local time, and solar longitude (Ls). Albedo input values were obtained from a 2 pixel per degree (ppd) TES global albedo map

(Kieffer, 2013). The KRC model has repeatedly been shown to successfully model complex surface types and thermophysical properties (e.g., Titus et al., 2003; Armstrong et al., 2005; Kieffer et al., 2006; Fergason et al., 2006a; 2006b; Edwards et al., 2009; Bandfield and Edwards, 2008; Bandfield and Feldman, 2008; Ahern et al., 2021).

Using viewing conditions identical to the ROTO observations, sets of simulated radiance spectra at varying TI values were created in KRC for each ROTO emission angle. To model surface emissivity, spectral features matching that of the surface composition are added to the simulated radiance spectra. Due to the lack of measured spectral features and relatively high dust abundance (Bandfield et al., 2002) at study site 1, surface emissivity is assumed to be that of surface dust, which is relatively featureless and contributes only a slight spectral slope (Bandfield et. al., 2000; Bandfield and Smith, 2003; Bandfield, 2009). To add these spectral features, the KRC-derived radiance spectra are multiplied by the emissivity spectrum of surface dust acquired from averaged Martian high albedo surfaces (Bandfield and Smith, 2003). Finally, the simulated surface emissivity was then calculated by dividing the simulated radiance by the Planck radiance at the THEMIS band 3. This method of emissivity separation is identical to the one applied to THEMIS measured radiance, allowing for a direct comparison (Bandfield, 2009).

If surface temperatures are too cold to allow for accurate emissivity retrieval, brightness temperature is calculated for bands 3 and 9. THEMIS BT measured at band 9 is compared to the modeled brightness temperature calculated from the KRC-derived spectral radiance. As band 9 is the most atmospherically transparent, the band 9 derived brightness temperature is considered the closest to the kinetic surface temperature. Here, we use the BT difference between bands 3 and 9 as a proxy for spectral slopes in emission data and as an indicator of sub-pixel temperature mixing. Both apparent and simulated brightness temperatures are calculated using a lookup table

of calculated bolometric Planck radiances. In short, the look-up tables consist of the THEMIS filter functions convolved with the Planck curve (assuming an emissivity of unity). Measured radiance is passed through the look-up table to determine what temperature produces the measured radiance in each band. The highest brightness temperature is assumed to be equal to the true surface kinetic temperature, the function repeats to determine the emissivity, and in turn brightness temperature in each of the other THEMIS bands (Christensen et al., 2001)). Ultimately, both surface emissivity modeling and brightness temperature modeling provide a means to estimate the subpixel surface unit abundance. Rock abundance derived from spectral emissivity modeling is the preferred approach as it employs the entire THEMIS spectral range and provides greater leverage of the complete data compared to the brightness temperature approach.

3.4.1 Rock Abundance Modeling:

Larger relative proportions of visible (and less dust-covered) rock increase the magnitude of the spectral slopes. In other words, a larger proportion of a high TI, rocky surface, surrounded by low TI dust produces emission spectra with greater spectral slopes. Using this knowledge, synthetic emission spectra and brightness temperatures were modeled to evaluate the effects of anisothermality caused by differences in TI of the surface units observed at each ROTO viewing geometry. For colder surfaces, the wavelength possibilities are limited due to atmospheric emission (e.g., area 2) and the simpler two-band brightness temperature model is employed.

Because the TI of an object is dependent on its thermal conductivity, grain size can be inferred from an object's TI value. Lower TI indicates fine-grained material and higher TI values indicate larger grain sizes (Jakosky 1986; Dollfus and Deschamps, 1986; Ruff and Christensen, 2002; Nowicki and Christensen, 2007; Pipueux and Christensen, 2011; Ahern et al., 2021). At

the sub-pixel scale, surface unit discrimination is dependent on the temperature contrast between those surface units (Cowart and Rogers, 2021). Over the LTST of the eight ROTO overpasses (18-19h), the KRC (Kieffer, 2013) thermal model was used to predict the temperatures for surface units with TI values correlating to Martian dust (50 TIU), sand (214 TIU), duricrust (400 TIU), and rocks of 0.1-0.15 m (1250 TIU) (Golombek et al., 2003; Cowart and Rogers, 2021). At this LTST, surface units with TI values up to 1250 TIU are distinguishable from one another whereas TI values from 1250-2500 TIU produced inseparable surface temperatures (e.g., rocks > ~0.2 m) (Figure 5).

4. Results:

4.1 Brightness Temperature Results:

All images used in this study were collected at LTST between 18:00-19:00h with emission angles between 2° and 37°. However, due to the off-nadir geometry of the ROTO acquisitions, the effective phase angle between the solar incidence and emission angles ranges from 59° - to 139°. In study area 1, the eight post-sunset observations have temperature asymmetries about the -2° roll angle (effectively nadir) with the lowest temperatures recorded at the highest emission angles (33°, -31°). Negative roll angles, favor western facing slopes and show higher overall temperatures than the positive roll angles of a similar magnitude. This corresponds to slopes recently illuminated by the western setting sun. Study region 2 has lower overall surface brightness temperatures than area 1. A maximum BT of 191K at the -31° ROTO roll and a low of 187K at the +8° ROTO roll was observed (Figure 4). The ROTO roll angle of +8° shows the largest temperature difference between THEMIS bands 3 and 9 at ~5K and the smallest difference is observed in the -31° ROTO at ~2K. At study site 2, differences in BT

between spectral channels decrease as the viewing angle moves to the more extreme positive and negative roll angles indicating a decrease in anisothermality at higher emission angles. The opposite is observed in study area 1.

4.2 Surface Emissivity Results:

A six-pixel region of interest (ROI) within study area 1 was chosen where the surface temperatures remained well above the atmospheric temperatures in all the THEMIS ROTO images (Fig. 3). A consistent negative spectral slope is apparent in the extracted emission spectra from the ROI. Generally, ROTOs with a negative roll angle (-31°, -24°, -12°) show negative spectral slopes of a greater magnitude than those extracted from ROTOs with positive roll angles (+33°, +26°, +18°, +8°), the exception to this is the -2° (e.g., nadir) which displays the lowest magnitude spectral slope. Where comparing emission spectra from complementary ROTO angles (e.g., -31° and +33°, -24° and +26°, etc.), the endmember pairs (-31° and +33°) show the largest difference in spectral slopes, whereas intermediate pairs (-12° and +18°, -24° and +26°) show less of a difference (Figure 6). Where plotted together, the measured emissivity spectra may constitute a continuum of spectral slopes beginning at the -2° roll and ending at the -31° roll. As the spectral slope is directly correlated to the magnitude of sub-pixel temperature mixing within the instrument FOV, this observed range in slopes provides a valuable insight into surface conditions at each viewing geometry. Furthermore, it demonstrates that ROTO observations provide a comprehensive view of surface features below an instruments spatial resolution that would typically require repeat nadir observations over long timescales.

4.3 Rock Abundance Modeling:

Using the methods outlined in section 3.4.1, we analyzed the effects of sub-pixel anisothermality by forward-modeling the emissivity spectral slopes for a range of two-component surfaces. By varying the emission angle, the relative proportion of distinctly different surface units are apparent. For example, off-nadir emission angles are more effective at viewing the sides of warm rocks mantled or capped by dust. Where surface units exhibit significant differences in temperature, an increase in the magnitude of the spectral slopes is observed (i.e., cold dusty surfaces and warm rocks). Sand and dust contributions were varied from 60-95% with the respective rock and regolith components. The resulting mixed TI radiance spectra were converted to emissivity resulting in sloped emission spectra similar to the observed ROTO spectra. Using the resulting synthetic spectra, a rock abundance model was created to represent the abundance of different surface units present at each viewing geometry.

For site 1, model combinations containing varying percentages of rock (1250 TIU) and dust (50 TIU) produced mixtures that best matched the surfaces observed bulk TI and temperature. The simulated anisothermal emission spectra for study area 1 are shown in Figure 7. Emission spectral slope modeling indicates that the higher magnitude off-nadir rolls best match the higher rock abundance models. As rolls approach nadir the observed spectral slope decreases and more closely matches the lower rock abundance model. This supports our hypothesis that higher off-nadir emission angles are more effective at viewing the warm sides of dust capped rocks.

As the modeled percentage of rock vs dust increases, the modeled spectral slope increases. Our modeling predicts that this trend will continue until a maximum temperature difference is reached, under the ROTO observing conditions this occurs around 40% rock and

60% dust. At this point, the trend reverses, and the modeled spectral slope decreases. At higher rock percentages, the warm rock surfaces dominate the TIR radiance and the temperature difference between warm and cold surfaces decreases. Sloped emissivity spectra follow proportionately up to the point where a modeled surface containing 40/60 dust and rock has a nearly identical sloped emissivity spectra to that of a surface with 90/10 dust and rock (Figure 8). Modeled apparent brightness temperature and model integrated TI vary greatly for these two surfaces allowing for a differentiation between the two spectral slopes.

Due to the cold surface temperatures (<200 K), rock abundance is derived at study area 2 using brightness temperature modeling. Results indicate a mixture of low TI (50 TIU) dust and a duricrust-like surface (600 TIU) in a 75/25 ratio. This mixture produces a model-integrated (weighted average) TI of 187 TIU, close to the previous THEMIS-derived bulk TI for this region (185 ± 12 J m^{-2} K^{-1} $s^{-1/2}$) from Fergason (2014). The modeled brightness temperature range of 190 to 187 across bands 3-9 closely match the average measured brightness temperature between bands 3-9 of 193-187 K. Simulated TI mixtures were varied in increments of 10%. This resulted in a more drastic variation in the modeled brightness temperature and TI than seen in study area 1. For example, at study site 2 the rock abundance model produces a dust-to-duricrust ratio of 75/25 that fit the measured brightness temperature and derived TI. However, a change in that dust/duricrust ratio of +/- 5% resulted in a modeled TI that varied from THEMIS derived values by +/- 27 TIU and a modeled brightness temperature that varied from measured values by +/- 15 K. This indicates that while effective, rock abundance modeling based on differences in brightness temperature does not provide the same precision in percent cover as spectral slope modeling.

5. Discussion:

In the post-sunset observations investigated here, we proposed that the observed sub-pixel thermal heterogeneities result from mixtures of surface units with varying TI values cooling at different rates. At night, warmer temperatures represent surfaces dominated by a greater proportion of higher TI objects (rocks), whereas cooler temperatures represent an abundance of lower TI materials (dust or sand). After sunset, lower TI materials cool quickly and the higher TI materials retain heat longer, thus creating the observed anisothermality. Moreover, dusty surfaces that appear uniform in nadir data can change where measured with off-axis observations. Relatively thin dust coatings are shown to have markedly distinct effects on the underlying objects TI. Dust coatings, several hundred microns in thickness, can significantly lower TI values of underlying rocky material. This effect is more drastic in the dusk and nighttime hours where dust is quickly cooling. Coatings of 1 diurnal skin depth (~1cm) or greater can completely mask the underlying signature (Mellon and Putzig, 2007). Rocks capped with airfall dust may have sides that are relatively dust-free. It is these sides that are warmed by the pre-sunset sun and thus are accentuated in the ROTO data (Figure 9). This is evident by the increased magnitude of spectral slopes observed in the off-nadir emission data and associated derived higher rock abundance.

Temperature heterogeneities in daytime data due to surface roughness have also been shown to produce negatively sloped emission spectra (e.g., Bandfield and Edwards, 2008; Bandfield, 2009; Bandfield et al., 2015). Rough surfaces undergo disproportionate solar heating and self-shadowing compared with smooth surfaces. However, because the ROTO observations described here are conducted post-sunset, quantitative estimates of surface roughness cannot be assessed as the surface is in effect fully shadowed (e.g., Bandfield and Edwards, 2008).

Both surface roughness and TI differences similarly affect the TIR spectrum, however, disentangling these effects requires advanced spacecraft observations. For example, specifically timed overpasses where the region of study is observed under illumination and viewing conditions that limit the effects of roughness and the emitted radiance is the same regardless of morphology (Davidsson et al., 2015). Lunar work under similar conditions demonstrates that anisothermality due to surface roughness is limited to high angles of solar incidence and not significant after sunset (Bandfield et al., 2015). In this study, surface roughness, while likely present, has minimal impact on the emitted radiance and sloped spectra can be reproduced by temperature differences due to sub-pixel TI.

5.1 Comparison with previous rock abundance models

The THEMIS ROTO spectral variability observed between each spacecraft overpass is consistent with that of an anisothermal surface as described by Bandfield and Edwards (2008) and Bandfield (2009). The data from study area 1 most closely matched simulated anisothermal spectra from a surface with an average rock abundance of 18%. The -31° roll shows the largest magnitude spectral slope with an observable decrease in spectral slope as the roll angle moves towards a roll of -2°. Spectral slope modeling of the -31° roll requires a higher rock abundance of 30% (Figure 10). The variability in modeled rock abundance value with viewing geometry indicates that higher emission angles capture a greater relative proportion of high TI material than nadir viewing geometries. Prior rock abundance models describe a 3% -5% abundance of rocks with TI values above 1250 TIU for this study region (Christensen 1986, Nowicki and Christensen 2007) similar to the nadir abundance derived here. Based on the increased THEMIS spatial resolution and novel viewing geometry, we argue that the local rock abundance is likely higher, upwards of 30%, as seen in the modeling of off-nadir data.

Due to the sensitivity of the TIR spectrum, lower TI materials such as sand and duricrust can be modeled in addition to traditional rock abundance. Brightness temperature, modeling at study region 2, indicates a complex surface dominated by a dust mantled surface with TI properties akin to duricrust. At larger emission angles, brightness temperature differences decrease, equating to a slightly more uniform surface. This difference indicates a more isothermal surface at high solar incidence angles and may suggest inundation of higher TI units by fine grained material or an abundance of rocky material. At emission angles approaching 0°, the surface appears more anisothermal, indicated by the greater BT difference between THEMIS bands 3-9.

5.2 Comparison to Orbital Data:

5.2.1 Study Area 1

HiRISE image data of study area 1 shows a possible collapse feature located within the lower Medusae Fossae formation (Figure 11). The ROI for this area contains the steep sides of the collapse feature rim along a north-western facing slope. Along the rim, surface material appears dark with larger boulders interspersed and is consistent with the modeled higher rock abundance. The floor has aeolian bedforms, indicating the presence of material transported by wind.

Due to the collapse feature's north-west slope orientation, ROTO observations with greater negative rolls produce viewing geometries more perpendicular to the surface than the -2º and +8º observations. This effectively lowers the emission angle of surface units along the collapse feature slopes. This, combined with the higher rock abundance near the slope, produces a greater degree of checkerboard temperature mixing resulting in the modeled higher rock

abundance at negative roll angles. Based on the THEMIS-derived TI and observed aeolian features, we modeled the fine material to be sand and dust with a grain size up to 160μm (Figure 11a).

Large boulder sized material is apparent in HiRISE images but features of this size are indifferentiable from smaller cm to m size rocks within these data. Detection of rock size represented by the higher TI material is limited by the temperature separability at the observed LTST. TI modeling indicates that materials with TI values above ~1250 exhibit nearly identical temperatures at the time of ROTO overpasses (Figure 5). Therefore, the derived rock abundance discussed here contains an upper limit on rock size of 0.1-0.15m. This represents material well below the detection limit of HiRISE image data and likely is the dark material along the collapse features rim and floor (Figure 11b).

5.2.2 Study Area 2

CTX data of study area 2 shows a complex surface dominated by impact craters and aeolian material (Figure 12). At the Sub-100m scale the terrain appears mottled with numerous small craters. Aeolian ripples are visible in the floors of some craters and along smoother plains-like terrain. The Derived TI values of this region are low (185 TIU) suggesting the presence of abundant fine material. This is consistent with results from the TI modeling performed here, which indicated a 75/25 mixture of low TI material (50 TIU) and moderate TI material (600 TIU). Based on the endmembers used in the TI mixing model we interpret this as regolith or poorly cemented rock heavily mantled by dust. Additionally, Crater rims and ejecta blankets have been shown to exhibit higher TI values than surrounding terrain (Mellon et al., 2000; Beddingfield et al., 2018). Tight groupings of impact craters, impacting into the same target substrate appear to behave similarly and show TI variation as a function of age and degradation

(Beddingfield et al., 2021). The numerous small craters and their ejecta blankets seen at study area 2 likely represent a source of temperature variation at the THEMIS sub-pixel level and provide an alternate hypothesis for the observed anisothermality.

6. Conclusions:

Understanding the rock abundance of a planetary surface provides insight into the processes that have shaped it. Additionally, a planet's surface directly influences most remote sensing measurements, typically at scales well below the spatial resolution of the data. Due to the non-linear nature of Planck radiance as a function of temperature and wavelength, TIR spectroscopy provides a unique tool to determine sub-pixel surface properties. Negative spectral slopes in TIR emissivity data are attributed to an inaccurate representation of the pixel-integrated surface temperatures, either from an incorrect assumption of the maximum emissivity or of an anisothermal surface within the field of view (Bandfield, 2009). Surfaces with greater degrees of anisothermality typically have a greater degree of negative spectral slopes. Checkerboard mixing of surface units, below the spatial resolution of the data, creates anisothermality in nadir data due to differences in the thermophysical properties of surface units. Importantly, where viewed off-nadir, the resulting change in magnitude of the spectral slopes is diagnostic of the spatial distribution of surface units and their abundance. The use of off-nadir datasets provides an independent way to validate rock abundance modeling that previously only relied on nadir data. Moreover, the off-nadir data may provide more accurate values by detecting the sides of rocks not as heavily mantled by dust as the upper surfaces imaged by nadir observations.

Although high-resolution visible images provide a direct method for identifying surface rock abundance, THEMIS TIR data provide a much greater spatial coverage and a quantitative way to extract thermophysically distinct surface characteristics from orbital data (Bandfield and

Edwards, 2008; Bandfield, 2009, Cowart and Rogers, 2021). The surfaces observed in proximity to Apollinaris Mons, for example, show highly variable spectral slopes. Spectral slopes are dependent on viewing angle with higher emission angles providing the greatest exaggeration of anisothermal conditions and therefore the most negative spectral slope. Spectral slope modeling at each viewing angle shows a range in derived rock abundance with the maximum and minimum viewing angles (-31° & 0°) providing endmembers at rock abundances of 30% and 5% respectively.

Relative rock abundance models do not provide a comprehensive characterization of surface properties; however, in conjunction with high-resolution visible image data and knowledge of the TI and brightness temperature of the surface, they do provide a means to deduce regolith properties such as grain size, compaction/cementation, and surface units (Christensen, 1986). Utilizing the instrument pointing capabilities and higher spatial resolution of THEMIS, we estimate a local rock abundance approaching 30% compared to 3-5% derived from previous models using nadir viewing geometries (Christensen 1986; Nowicki and Christensen, 2007). The effectiveness of this new model results from the off nadir viewing geometry. Rocks mantled by optically thick surface dust, as thin as a few hundred microns, experience a reduction in TI. Whereas coatings of dust ~1cm in thickness can completely mask the rock signature. Where viewed from nadir these surfaces do not contribute to the emitted radiance where (Mellon et al., 2007). However, off-nadir viewing detects the relatively lower dust-covered sides of rocks, effectively revealing high TI targets in an otherwise dusty landscape.

Where atmospheric temperatures exceed surface temperatures traditional THEMIS IR atmospheric correction is not possible. However, in cases where surface emissivity cannot be

563 extracted due to complexities in surface/atmosphere temperature interactions, a two-point BT
564 comparison provides a valid alternative, albeit at a decreased precision. Brightness temperature
565 modeling at study area 2 indicates a complex surface containing a mixture of dust and duricrust-
566 like material in a 75/25 distribution. This is supported by CTX data showing abundant small
567 impact craters. This, along with the relatively low TI, suggests a heavily dust-covered surface but
568 enough cementation to support crater retention. Unlike study area 1, brightness temperature
569 differences are greatest at the nadir viewing geometry with more isothermal conditions seen at
570 higher emission angles. This indicates that the observed anisothermality is solely a function of
571 the surface's thermophysical properties and not a result of viewing geometry. Furthermore, it
572 demonstrates the effectiveness of THEMIS ROTO acquisitions to detect sub-pixel differences in
573 temperatures from overpasses collected in a relatively short time compared to the use of nadir
574 images acquired across multiple local solar times and seasons.

575 Investigations of anisothermality at sub-pixel scales are critical to understanding
576 planetary surfaces and give insight into the processes that shape them. This has been done
577 previously with nadir viewing TIR data on Mars and other planetary bodies (Nowicki and
578 Christensen 2007; Bandfield and Edwards, 2008; Bandfield, 2009; Cowart and Rogers, 2021).
579 However, the derived rock abundance estimates enabled by the ROTO measurements are four
580 orders of magnitude greater than previous rock abundance estimates using nadir TIR data. They
581 also provide measurements of surfaces not prone to airfall dust cover, which may be important
582 for improving the accuracy of thermophysical and compositional studies. Additionally, the
583 sensitivity of the TIR data is an order a magnitude improvement in scale over radar and visible
584 imaging of the surface. Finally, the unique aspect of ROTOs provides a novel opportunity to re-

585 interpret a surface, revealing previously undetected features at fine scales. This not only aids in
586 geologic interpretation but can provide the groundwork for future exploration.

587 **Acknowledgments**

588 The authors would like to recognize Josh Bandfield who directly influenced the work
589 presented here. Thank you to Deanne Rogers, Vicky Hamilton, Kimm Murray, and Jonathan Hill
590 who provided direction and guidance on THEMIS TIR image data corrections. Thank you to the
591 members of the THEMIS off-nadir working group whose hard work and planning went into the
592 acquisition of the ROTO data. This work was supported by the NASA Mars Odyssey Project and
593 Participating Scientist Program awarded to MSR.

594

595 **Open Research**

596 This work includes data from multiple instruments, spread across multiple sources, as
597 well as modeling code and results. All THEMIS can be found on the appropriate Data Node
598 under the Planetary Data System (http://viewer.mars.asu.edu/viewer/themis#T=0) by searching
599 for the image ID numbers *(I86177001, I86202001, I85939006, I85964009, I85989005,*
600 *I86014012, I86039007, I86064009).* MRO CTX and HiRISE images are available from the Mars
601 Orbital Data Explorer (https://ode.rsl.wustl.edu/mars/index.aspx) under the Planetary Data
602 System Geosciences Node by searching for the image ID numbers
603 (*B05_011653_1714_XN_08S186W, ESP_047230_178).* The KRC thermal model is freely
604 available from Arizona State University and can be found at http://krc.mars.asu.edu with detailed
605 instructions on how to download, install, and run the model. The Davinci interface for spectral
606 processing and KRC can be downloaded from http://davinci.asu.edu . Spectral Libraries used in
607 the modeling and atmospheric correction as well as all raw results from the KRC model and

image data are available in the repository McKeeby et al., 2022 Apollinaris, Zenodo (10.5281/zenodo.6522670).

References

Ahern, A. A., Rogers, A. D., Edwards, C. S., & Piqueux, S. (2021). Thermophysical properties and surface heterogeneity of landing sites on Mars from overlapping Thermal Emission Imaging System (THEMIS) observations. *Journal of Geophysical Research: Planets*, 126(6), e2020JE006713.

Armstrong, J. C., Titus, T. N., & Kieffer, H. H. (2005). Evidence for subsurface water ice in Korolev crater, Mars. *Icarus*, 174(2), 360-372.

Aufaristama, M., Höskuldsson, Á., Ulfarsson, M. O., Jónsdóttir, I., & Thordarson, T. (2020). Lava Flow Roughness on the 2014–2015 Lava Flow-Field at Holuhraun, Iceland, Derived from Airborne LiDAR, and Photogrammetry. *Geosciences*, *10*(4), 125.

Bandfield, J.L., (2009), Effects of Surface Roughness and Graybody Emissivity on Martian Thermal Infrared Spectra, *Icarus*, 202,414-428, https://doi.org/10.1016/j.icarus.2009.03.031.

Bandfield, J. L. (2006). Extended surface exposures of granitoid compositions in Syrtis Major, Mars. *Geophysical research letters*, 33(6).

Bandfield, J. L. (2008). High-silica deposits of an aqueous origin in western Hellas Basin, Mars. *Geophysical Research Letters*, 35(12).

Bandfield, J.L., & C.S. Edwards, (2008). Derivation of Martian surface slope characteristics from directional thermal infrared radiometry, *Icarus*, 10.1016/j.icarus.2007.08.028.

Bandfield, J. L., & Feldman, W. C. (2008). Martian high latitude permafrost depth and surface cover thermal inertia distributions. *Journal of Geophysical Research: Planets*, 113(E8).

Bandfield, J. L., & Rogers, A.D., (2020). Thermal infrared spectral modeling, In: J. Bishop, J. Moersch, and J. F. Bell III (Eds.) *Remote Compositional Analysis*, Cambridge University Press, Cambridge, 10.1017/9781316888872.

Bandfield, J. L., & Smith, M. D. (2003). Multiple emission angle surface–atmosphere separations of Thermal Emission Spectrometer data. Icarus, 161(1), 47-65.

Bandfield, J. L., Christensen, P. R., & Smith, M. D. (2000). Spectral data set factor analysis and end-member recovery: Application to analysis of Martian atmospheric particulates. *Journal of Geophysical Research: Planets*, 105(E4), 9573-9587.

Bandfield, J.L., P.O. Hayne, J.-P. Williams, B.T. Greenhagen, D.A. Paige, (2015). Lunar surface roughness derived from LRO Diviner Radiometer observations, *Icarus*, 10.1016/j.icarus.2014.11.009.

Bandfield, J. L., Rogers, D., Smith, M. D., and Christensen, P. R. (2004). Atmospheric correction and surface spectral unit mapping using Thermal Emission Imaging System data, *Journal of Geophysical Research*, 109, E10008, doi:10.1029/2004JE002289.

Beddingfield, Chloe B., Jeffrey E. Moersch, and Harry Y. McSween Jr. "Investigating crater rim thermal inertia variations on Mars: A case study in Tisia Valles." *Icarus* 314 (2018): 345-363.

Beddingfield, Chloe B., Jeffrey E. Moersch, and Harry Y. McSween Jr. "The relationship between thermal inertia and degradation state of craters in areas of low surface dust cover on Mars." *Icarus* 370 (2021): 114678.

Bradley, B. A., Sakimoto, S. E., Frey, H., & Zimbelman, J. R. (2002). Medusae Fossae Formation: New perspectives from Mars Global Surveyor. *Journal of Geophysical Research: Planets*, 107(E8), 2-1.

Burr, D.M., Enga, M.-T., Williams, R.M.E., Zimbelman, J.R., Howard, A.D., Brennand, T.A (2009). Pervasive aqueous paleoflow features in the Aeolis/Zephyria Plana region, Mars, *Icarus*, 200(1), 52-76

Campbell, B. A., & Shepard, M. K. (1996). Lava flow surface roughness and depolarized radar scattering. *Journal of Geophysical Research: Planets*, *101*(E8), 18941-18951.

Carter, A.J., Ramsey, M.S., Durant, A.J., Skilling, I.P., Wolfe, A.L., (2009) Micron-scale roughness of volcanic surfaces from thermal infrared spectroscopy and scanning electron microscopy, *Journal of Geophysical. Research*, 114, B02213, doi:10.1029/2008JB005632.

Christensen, P. R. (1986), The spatial distribution of rocks on Mars, *Icarus*, 68, 217– 238, doi:10.1016/0019-1035(86)90020-5.

Christensen, P. R., Jakosky, B. M., Kieffer, H. H., Malin, M. C., McSween, H. Y., Nealson, K., ... & Ravine, M. (2004). The thermal emission imaging system (THEMIS) for the Mars 2001 Odyssey Mission. *Space Science Reviews*, 110(1), 85-130.

Chuang, F. C., Crown, D. A., & Berman, D. C. (2019). Geology of the northeastern flank of Apollinaris Mons, Mars: Constraints on the erosional history from morphology, topography, and crater populations. *Icarus*, 333, 385-403.

Cowart, J. C., & Rogers, A. D. (2021). Investigating Sources of Spectral Olivine Enrichments in Martian Bedrock Plains Using Diurnal Emissivity Changes in THEMIS Multispectral Images. *Journal of Geophysical Research: Planets*, 126(11), e2021JE006947.

Crown, D. A., & Ramsey, M. S. (2017). Morphologic and thermophysical characteristics of lava flows southwest of Arsia Mons, Mars. *Journal of volcanology and geothermal research*, 342, 13-28.

Davidsson, B. J., Rickman, H., Bandfield, J. L., Groussin, O., Gutiérrez, P. J., Wilska, M., ... & Mueller, T. G. (2015). Interpretation of thermal emission. I. The effect of roughness for spatially resolved atmosphereless bodies. *Icarus*, 252, 1-21.

Edwards, C. S., Bandfield, J. L., Christensen, P. R., & Fergason, R. L. (2009). Global distribution of bedrock exposures on Mars using THEMIS high-resolution thermal inertia. *Journal of Geophysical Research-Planets*, *114*, 18. E11001, doi: 10.1029/2009je003363

Ewing, R. C., Lapotre, M. G. A., Lewis, K. W., Day, M., Stein, N., Rubin, D. M., ... & Fischer, W. W. (2017). Sedimentary processes of the Bagnold Dunes: Implications for the eolian rock record of Mars. *Journal of Geophysical Research: Planets*, 122(12), 2544-2573.

Fergason, R.L., (2014) Thermal Inertia Mosaic Quantitative Map from 30S to 240E, *USGS Astrogeology Science Center*.

Fergason, R. L., P. R. Christensen, and H. H. Kieffer (2006a), High-resolution thermal inertia derived from the Thermal Emission Imaging System (THEMIS): Thermal model and applications, *Journal of Geophysical Reseach*, 111, E12004, doi:10.1029/2006JE002735.

Fergason, R. L., Christensen, P. R., Bell III, J. F., Golombek, M. P., Herkenhoff, K. E., & Kieffer, H. H. (2006b). Physical properties of the Mars Exploration Rover landing sites as inferred from Mini-TES–derived thermal inertia. *Journal of Geophysical Research: Planets*, 111(E2).

Gillespie, A. R., A. B. Kahle, and R. E. Walker (1986), Color enhancement of highly correlated images: I. Decorrelation and HIS contrast stretches, *Remote Sensing of the Environment*, 20, 209– 235.

Howard, A. D. (1981). Etched plains and braided ridges of the south polar region of Mars: Features produced by basal melting of ground ice? *Reports of Planetary Geology Program*, 286-288.

Hynek, B. M., Phillips, R. J., & Arvidson, R. E. (2003). Explosive volcanism in the Tharsis region: Global evidence in the Martian geologic record. *Journal of Geophysical Research: Planets*, 108(E9).

Jakosky, B. M., Finiol, G. W., & Henderson, B. G. (1990). Directional variations in thermal emission from geologic surfaces. *Geophysical Research Letters*, 17(7), 985-988.

Jones, E., Caprarelli, G., and Osinski, G. R. (2016), Insights into complex layered ejecta emplacement and subsurface stratigraphy in Chryse Planitia, Mars, through an analysis of THEMIS brightness temperature data, *Journal of Geophysical Research: Planets*, 121, 986– 1015, doi:10.1002/2015JE004879.

Kerber, L., & Head, J. W. (2010). The age of the Medusae Fossae Formation: Evidence of Hesperian emplacement from crater morphology, stratigraphy, and ancient lava contacts. *Icarus*, 206(2), 669-684.

Kieffer, H. H. (2013). Thermal model for analysis of Mars infrared mapping. *Journal of Geophysical Research: Planets*, 118(3), 451-470.

Kieffer, H. H., Martin, T. Z., Peterfreund, A. R., Jakosky, B. M., Miner, E. D., and Palluconi, F. D. (1977), Thermal and albedo mapping of Mars during the Viking primary mission, *Journal of Geophysical Research*, 82 (28), 4249–4291, doi:10.1029/JS082i028p04249.

Kieffer, H. H., Christensen, P. R., & Titus, T. N. (2006). CO 2 jets formed by sublimation beneath translucent slab ice in Mars' seasonal south polar ice cap. *Nature*, 442(7104), 793-796.

Lane, M. D., & Christensen, P. R. (1998). Thermal infrared emission spectroscopy of salt minerals predicted for Mars. *Icarus*, *135*(2), 528-536.

Mandt, K. E., de Silva, S. L., Zimbelman, J. R., & Crown, D. A. (2008). Origin of the Medusae Fossae Formation, Mars: Insights from a synoptic approach. *Journal of Geophysical Research: Planets*, 113(E12).

McEwen, A. S., Eliason, E. M., Bergstrom, J. W., Bridges, N. T., Hansen, C. J., Delamere, W. A., ... & Weitz, C. M. (2007). Mars reconnaissance orbiter's high resolution imaging science experiment (HiRISE). *Journal of Geophysical Research: Planets*, 112(E5).

McKeeby, B.E. and Ramsey, M.S., (2020) Spectral anisothermality: A two-look approach to thermal infrared data analysis of planetary basaltic surfaces, *51st Lunar Planetary Science Conference*, abs. #2083.

McKeeby, B.E., and Ramsey, M.S., (2021) Deriving planetary surface roughness: Combining digital photogrammetry and thermal infrared spectroscopy. *52nd Lunar Planetary Science Conference*, abs. #1957.

Mellon, M.T., Jakosky, B.M., Kieffer, H.H., Christensen, P.R., (2000) High-Resolution Thermal Inertia Mapping from the Mars Global Surveyor Thermal Emission Spectrometer, *Icarus*, 148 (2), 437-455, https://doi.org/10.1006/icar.2000.6503.

Mellon, M. T., and N. E. Putzig. "The apparent thermal inertia of layered surfaces on Mars." *Lunar and planetary science conference*. No. 1338. 2007.

Mustard, J. F., and T. D. Glotch (2019), Theory of Reflectance and Emittance Spectroscopy of Geologic Materials in the Visible and Infrared Regions, In: J. Bishop, J. Moersch, and J. F. Bell III (Eds.) *Remote Compositional Analysis*, p21-41, Cambridge University Press, Cambridge, doi:10.1017/9781316888872.004.

771 Palluconi, F.D., & Kieffer, H.H. (1981). Thermal Inertia Mapping of Mars from 60 deg S to 60 deg N, *Icarus*, 45,
772 415-426.
773
774 Putzig, N.E., Mellon, M.T., Kretke, K.A., Arvidson, R.E., (2005) Global Thermal Inertia and Surface Properties of
775 Mars from the MGS mapping Mission, *Icarus*, 173 (2), 325-341.
776
777 Ramsey, M.S., and Fink, J.H., (1999) Estimating silicic lava vesicularity with thermal remote sensing: A new
778 technique for volcanic mapping and monitoring, *Bulletin of Volcanology*, 61, 32-39.
779
780 Rose, S.R., Watson, W., Ramsey, M.S., Hughes, C.G., (2014) Thermal Deconvolution: Accurate retrieval of
781 Multispectral Infrared Emissivity from Thermally-Mixed Volcanic Surfaces, *Remote Sensing of the Environment*,
782 140, pp 690-703. https://doi.org/10.1016/j.rse.2013.10.009.
783
784 Ruff, S. W., Christensen, P. R., Barbera, P. W., & Anderson, D. L. (1997). Quantitative thermal emission
785 spectroscopy of minerals: A laboratory technique for measurement and calibration. *Journal of Geophysical*
786 *Research: Solid Earth*, *102*(B7), 14899-14913.
787
788 Sanchez-Vahamonde, C. R., & Neish, C. (2021). The Surface Texture of Martian Lava Flows as Inferred from Their
789 Decimeter-and Meter-scale Roughness. *The Planetary Science Journal*, *2*(1), 15.
790
791 Scott, D. H., & Tanaka, K. L. (1986). Geologic map of the western equatorial region of Mars.
792
793 Shepard, M. K., Campbell, B. A., Bulmer, M. H., Farr, T. G., Gaddis, L. R., & Plaut, J. J. (2001). The roughness of
794 natural terrain: A planetary and remote sensing perspective. *Journal of Geophysical Research: Planets*, 106(E12),
795 32777-32795.
796
797 Simurda, C. M., Ramsey, M. S., & Crown, D. A. (2019). The unusual thermophysical and surface properties of the
798 Daedalia Planum lava flows. *Journal of Geophysical Research: Planets*, *124*(7), 1945-1959.
799
800 Smith, M. D., Bandfield, J. L., & Christensen, P. R. (2000). Separation of atmospheric and surface spectral features
801 in Mars Global Surveyor Thermal Emission Spectrometer (TES) spectra. *Journal of Geophysical Research: Planets*,
802 105(E4), 9589-9607.
803
804 Smith, M. D., J. L. Bandfield, P. R. Christensen, and M. I. Richardson (2003), Thermal Emission Imaging System
805 (THEMIS) infrared observations of atmospheric dust and water ice cloud optical depth, *Journal of Geophysical*
806 *Research*, 108(E11), 5115, doi:10.1029/2003JE002115.
807
808 Tanaka, K. L. (2000). Dust and ice deposition in the Martian geologic record. *Icarus*, 144(2), 254-266.
809
810 Titus, T. N., Kieffer, H. H., & Christensen, P. R. (2003). Exposed water ice discovered near the south pole of Mars.
811 *Science*, 299(5609), 1048-1051.
812
813 Voigt J.R.C., Hamilton C.W., (2021a). Facies map for the 2014–2015 Holuhraun eruption in Iceland. In: University
814 of Arizona, Department of Planetary Sciences, Lunar and Planetary Laboratory.
815 https://doi.org/10.25422/azu.data.12971129.v3
816
817 Voigt, J. R., Hamilton, C. W., Steinbrügge, G., & Scheidt, S. P. (2021b). Surface roughness characterization of the
818 2014–2015 Holuhraun lava flow-field in Iceland: implications for facies mapping and remote sensing. *Bulletin of*
819 *Volcanology*, *83*(12), 1-14.
820
821 Whelley P.L., Garry W.B., Hamilton C.W., Bleacher J.E. (2017), LiDAR-derived surface roughness signatures of
822 basaltic lava types at the Muliwai a Pele Lava Channel, Mauna Ulu, Hawai'i. *Bulletin of Volcanology*, 79(11):75
823
824 Whelley P.L., Glaze L.S., Calder E.S., Harding D.J. (2014), LiDAR-derived surface roughness texture mapping:
825 application to Mount St. Helens Pumice plain deposit analysis. *IEEE Transactions Geoscience Remote Sensing*,
826 52(1):426–438

Whitney, M. I. (1985). Yardangs. *Journal of Geological Education*, 33(2), 93-96.

Williams, R. M. E., & Edgett, K. S. (2005). Valleys in the Martian rock record. *Lunar and Planetary Science* 36, abs#1099.

Zimbelman, J. R., & Griffin, L. J. (2010). HiRISE images of yardangs and sinuous ridges in the lower member of the Medusae Fossae Formation, Mars. *Icarus*, 205(1), 198-210.

Zimbelman, J.R., and Scheidt, S.P., (2018). Geologic maps of Mars quadrangles MC-23 NW and MC-16 NW. *Scientific Investigations Map*, scale 1:2M, U.S. Geological

839 **Figures and Tables:**

840

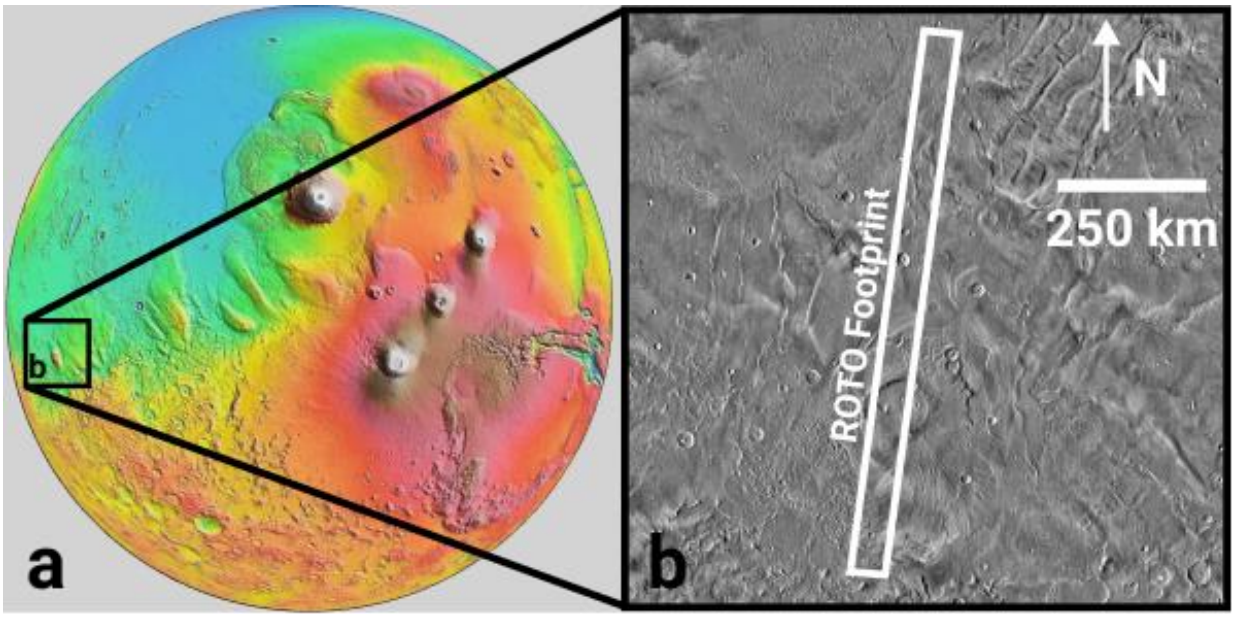

Figure 1. a) Map of Mars showing the location of the study region near Apollinaris Mons. b) THEMIS day IR with the March 2021 ROTO footprint shown.

841

THEMIS Image ID	***Roll Angle***	***Emission Angle***	***Solar Longitude (Ls)***	***Local Time (True)***
I86177001	-31	35.3	47.0	18.2
I86202001	-24	27.2	47.9	18.3
I85939006	-12	13.4	38.3	18.3
I85964009	-2	2.6	39.2	18.4
I85989005	8	10.2	40.2	18.5
I86014012	18	20.3	41.1	18.6
I86039007	26	29.4	42.0	18.6
I86064009	33	37.5	42.9	18.7

Table 1. Data specific parameters of the eight ROTO images acquired for this study.

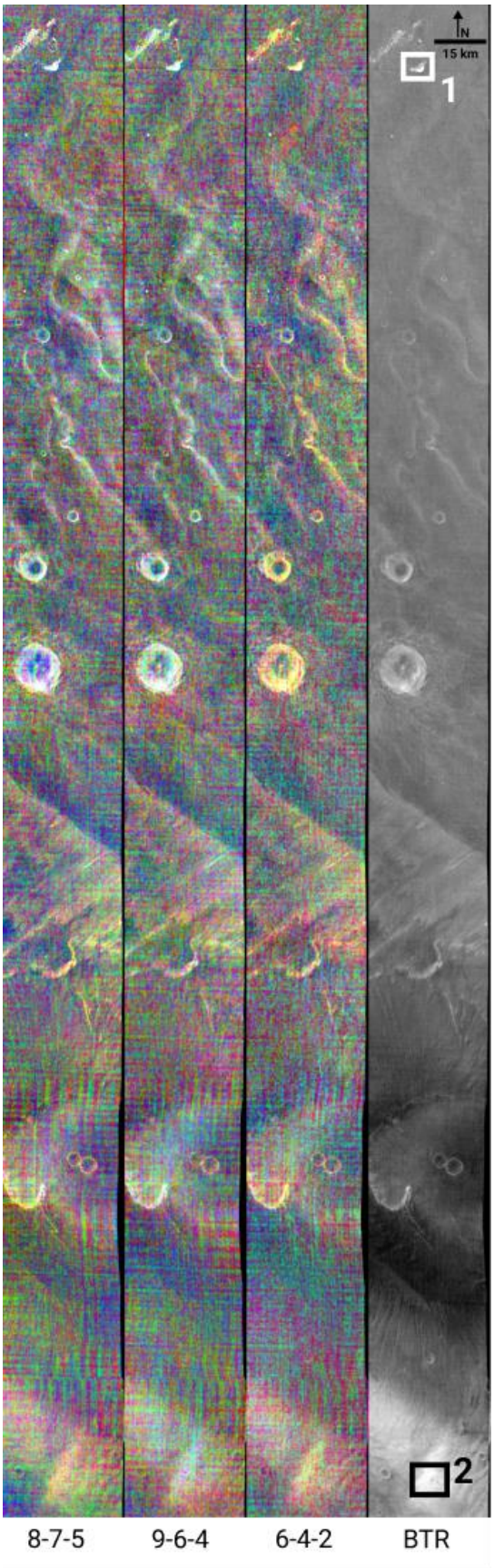

Figure 2. THEMIS 4-panel plot of the ROTO data (ID# I86177001) covering the region north of Apollinaris Mons and centered near 174° E, 8° S. The three left images are DCS images of THEMIS radiance using bands 8-7-5, 9-6-4, and 6-4-2, respectively. The fourth image is the derived brightness temperature. Study areas 1 and 2 are shown by the white boxes.

842

843

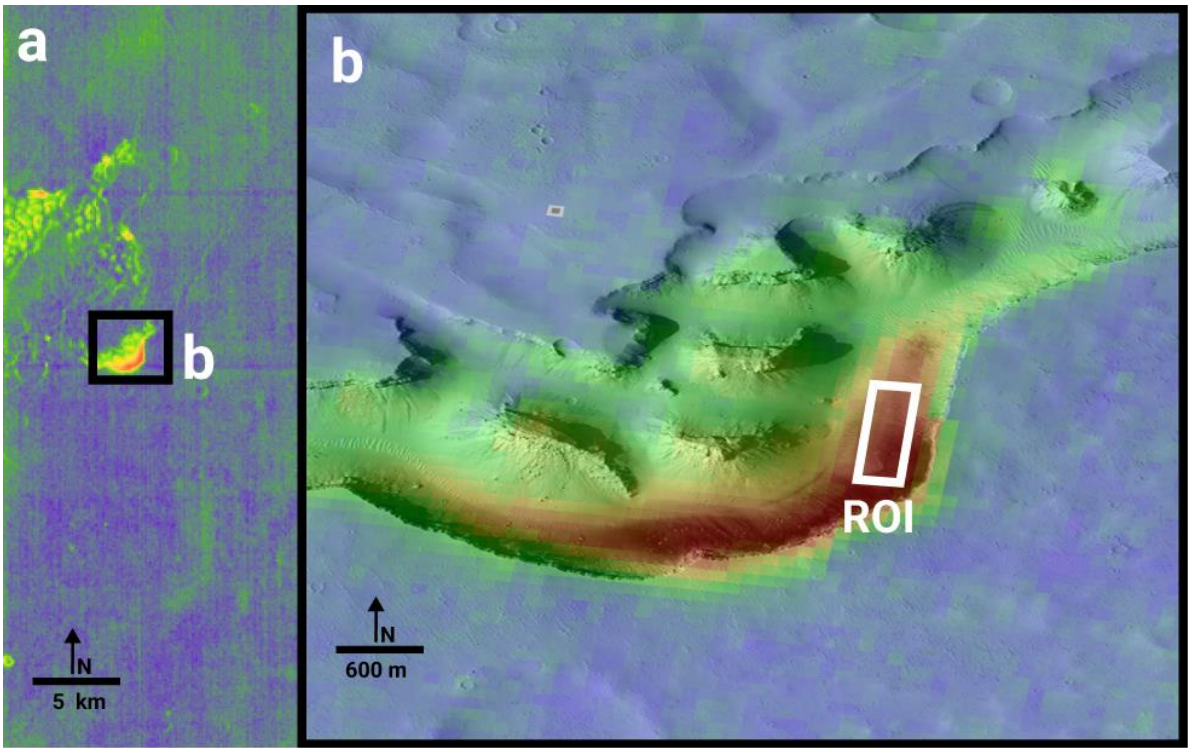

Figure 3. a) Colorized BTR image showing study area 1. Higher temperatures indicated by warmer colors. b) Colorized BTR image overlain on HiRISE image ESP_047230_178. White box indicates ROI used for spectral emissivity extraction.

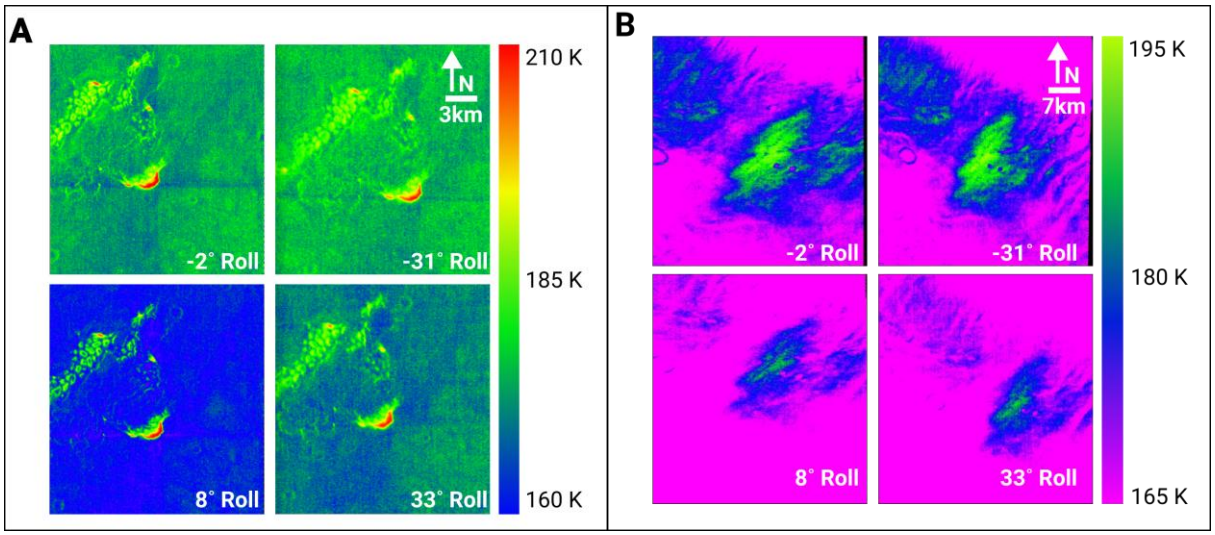

Figure 4. Colorize brightness temperature images at study areas 1(A) and 2(B) demonstrating the change in observed brightness temperature as a function of emission angle. Endmember ROTOs at rolls of -2º, -31º, +8º, and +33º are shown.

844

845

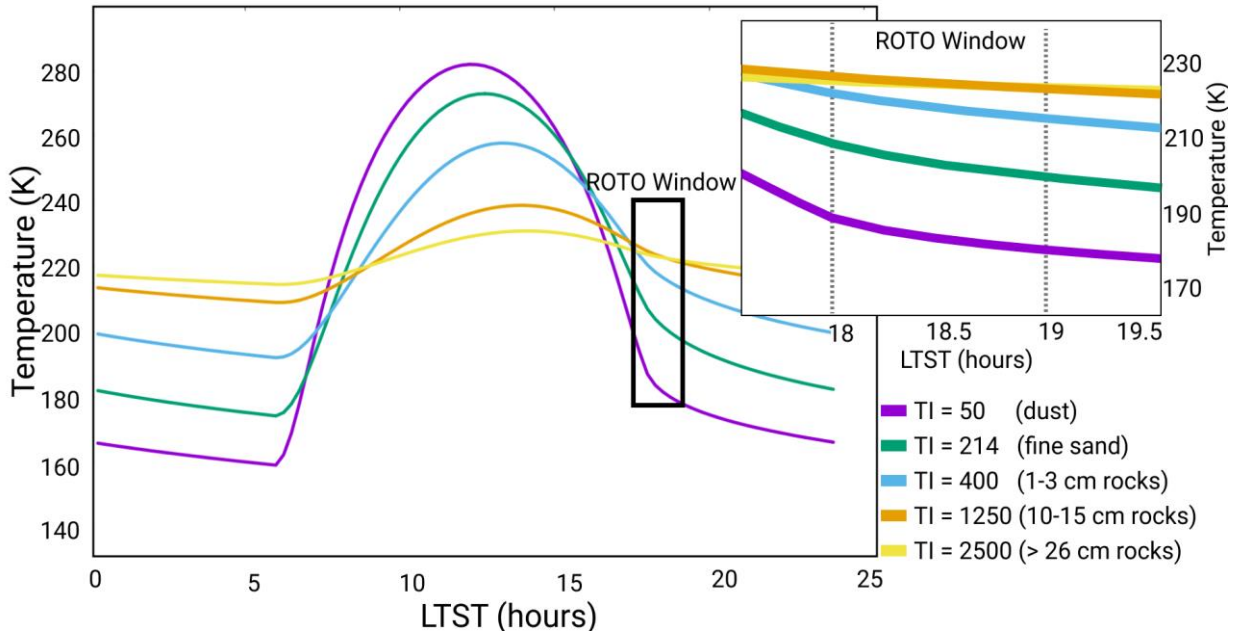

Figure 5. Diurnal curve of different materials with TI values ranging from 50-2500 TIU. Surface units with TI values above 1250 TIU produce temperatures indistinguishable from one another and are inseparable in sub-pixel mixture modeling.

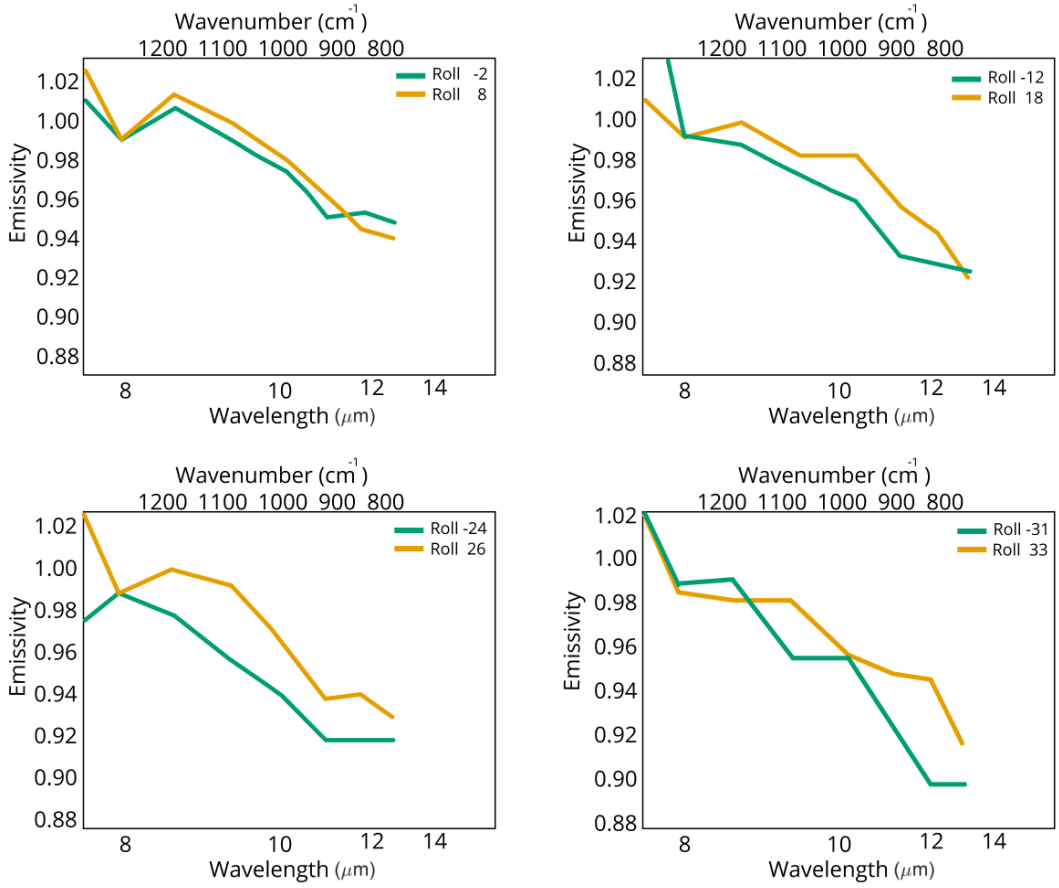

Figure 6: THEMIS emission spectra from each paired ROTO observation acquired over the ROI in Figure 3. Endmember roll angles (-31° and +33°, -2° and +8°) show the largest difference in spectral slope, whereas intermediate roll angles (-12° and +18°, -24° and +26°) show the smallest difference.

846

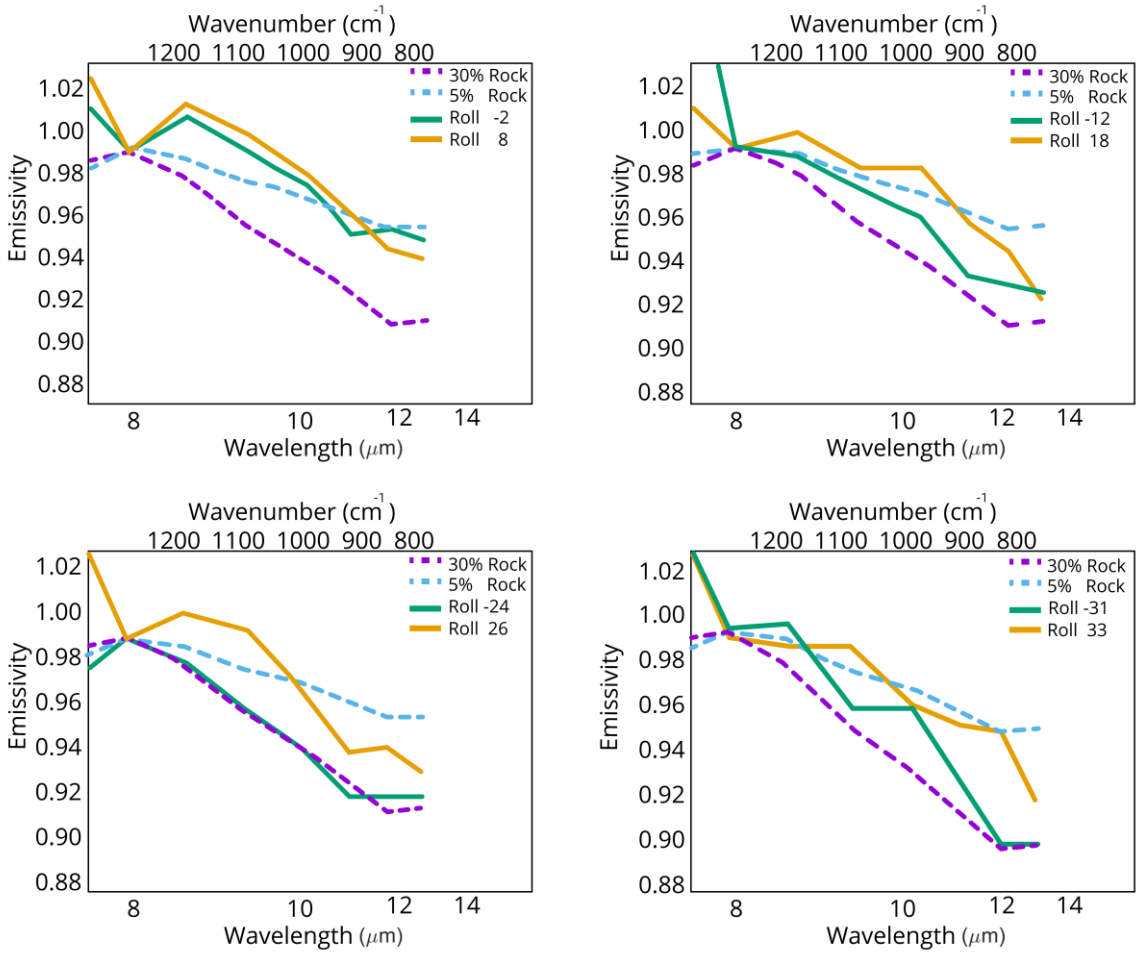

Figure 7. Simulated surface emissivity spectra modeled using the viewing parameters from Study Area 1 listed in Table 1. Spectra for 8 different viewing geometries are shown. A Martian dust spectrum was convolved with the modeled blackbody spectrum to add "spectral color." The negative spectral slopes are due to differences in temperature caused by varying distributions TI units at each viewing geometry.

847

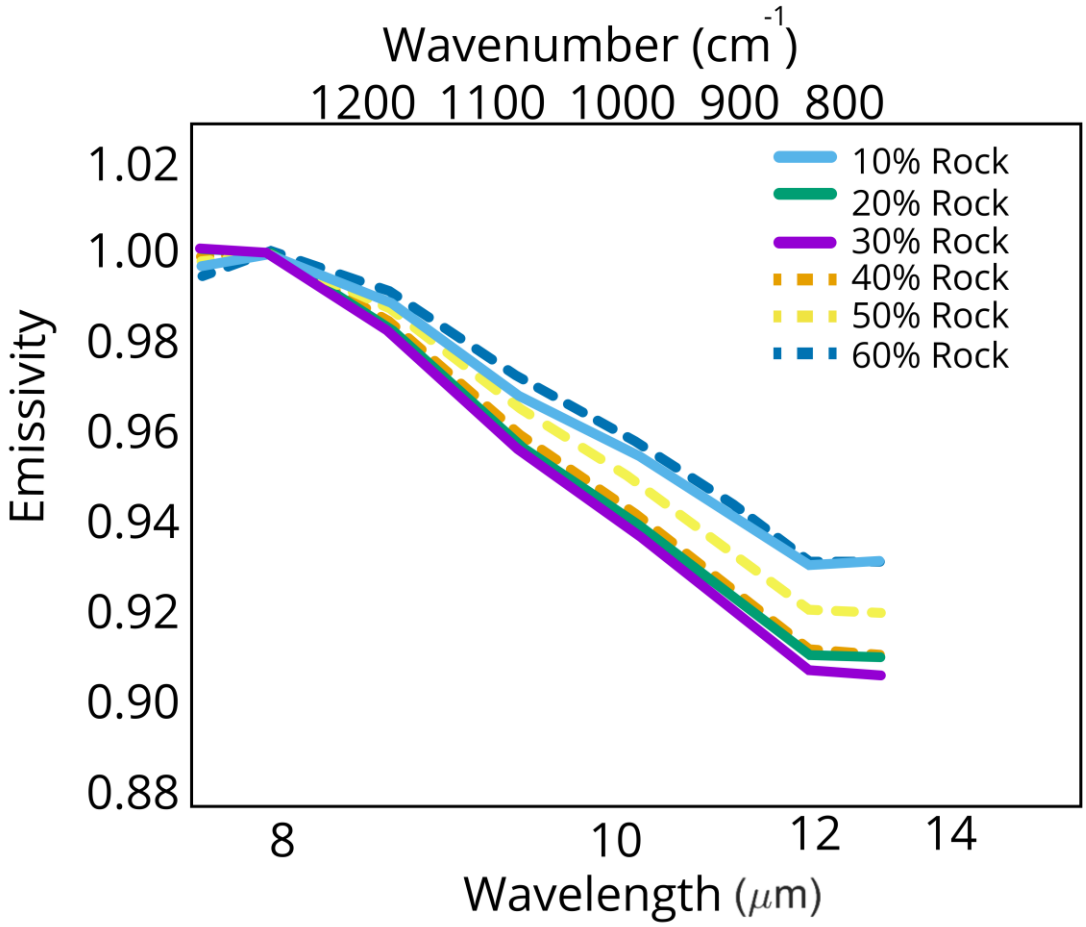

Figure 8. Synthetic emission slopes created for varying mixtures of rock and dust. The addition of greater percentage of rock into the mixture results in an increase in the spectral slope until a ratio of 30/70 rock to dust is reached. After this point the trend reverses and spectra become less sloped.

848
849

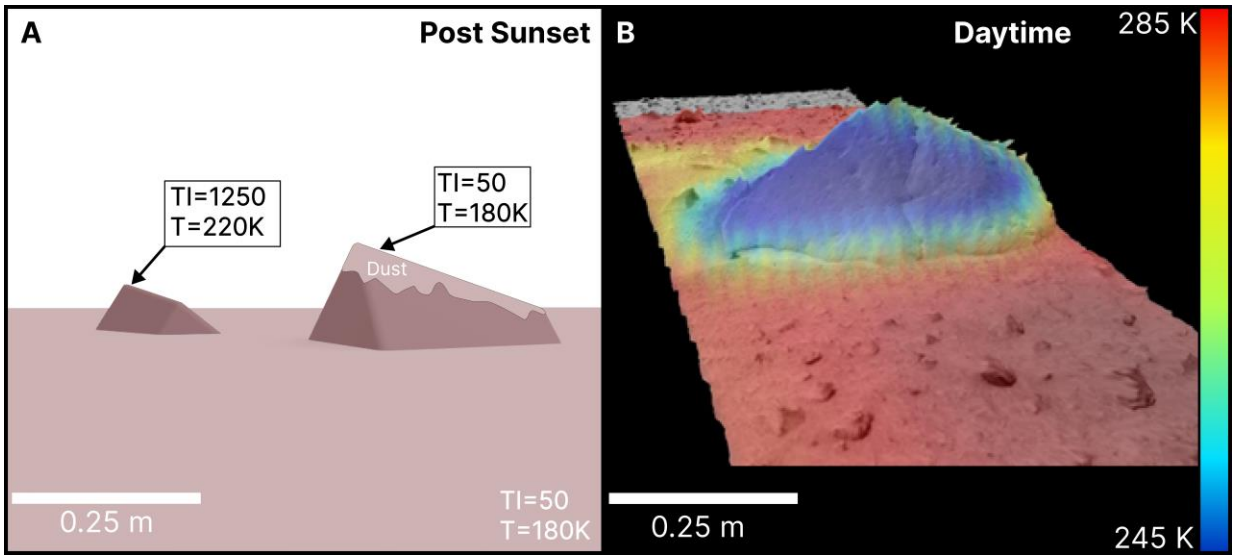

Figure 9. A) Schematic demonstrating the expected temperature differences between less dusty rock sides vs the dust capped top in post sunset. B) Colorized daytime Mini-TES temperature image from the Spirit rover of the basaltic rock "Adirondack." In daytime observations, high TI materials (rocks) appear colder compared to surrounding low TI materials.

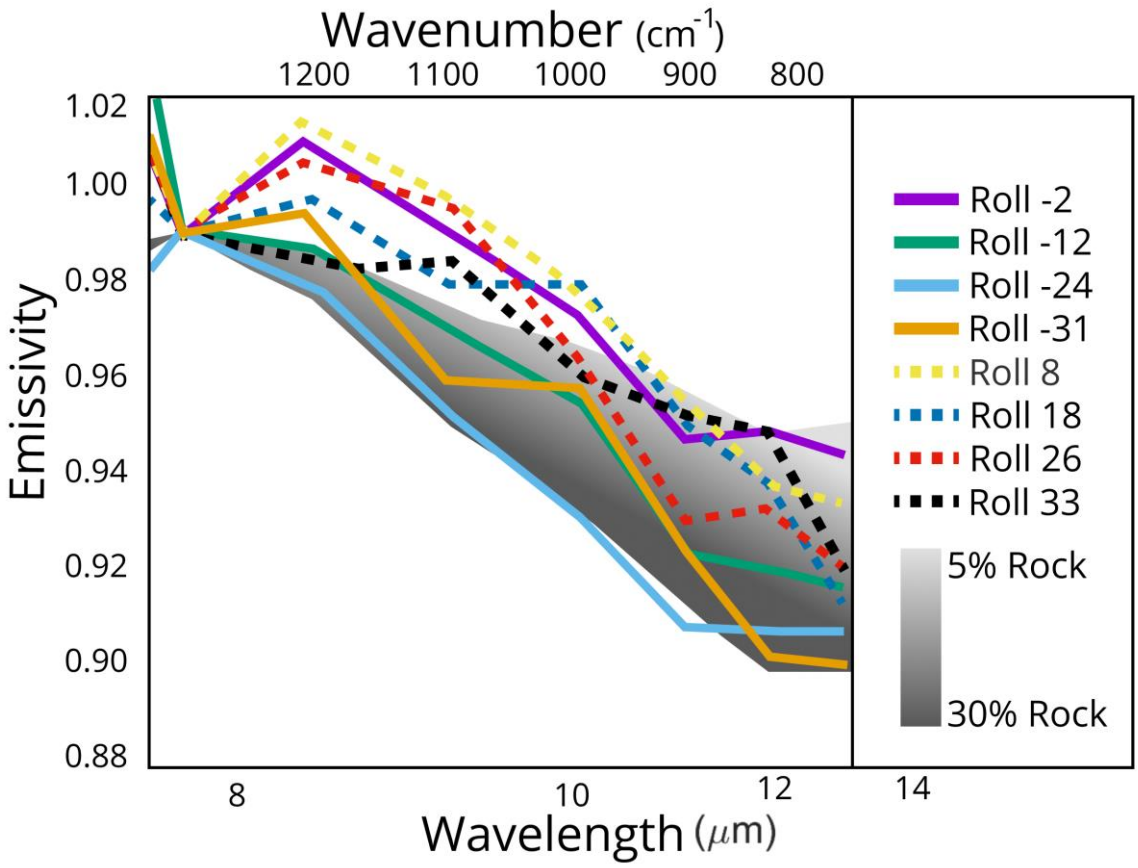

Figure 10. All THEMIS surface emissivity spectra from the collapse feature in study area 1 at each viewing angle. Negative ROTO angle observations are shown in solid lines and positive ROTO angle observations are shown as dotted. The shaded region denotes the range of spectral slopes equating to the modeled TI mixtures. The variability in spectral slopes is a result of differences in the relative distribution of high and low TI units in the FOV of each observation. Positive rolls exhibit generally higher emissivity, indicating less temperature mixing and a lower modeled rock abundance.

854

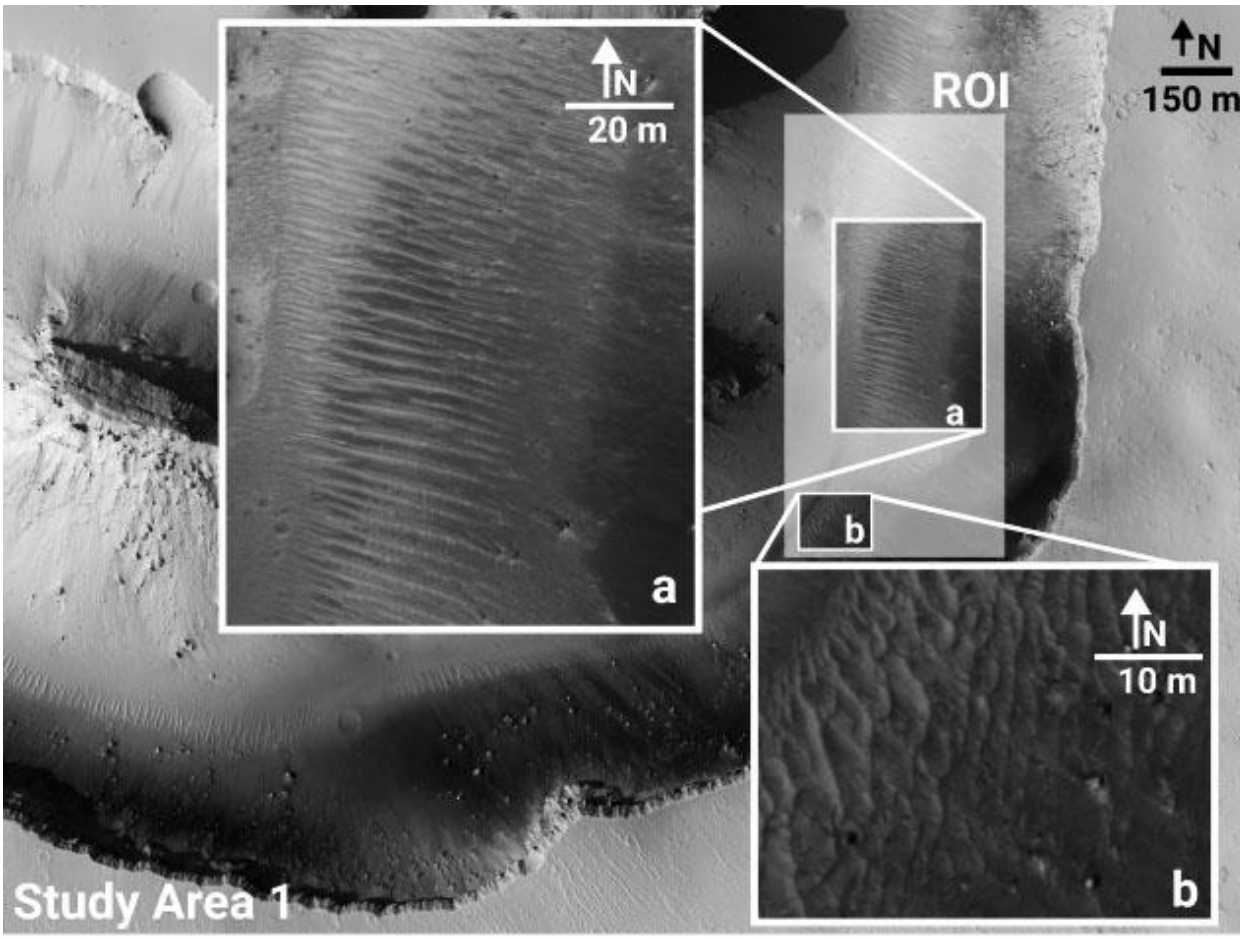

Figure 11. HiRISE image ESP_047230_178 of study area 1 showing the THEMIS ROI footprint in the shaded region. Areas A and B show aeolian bedforms and larger boulders interspersed within the ROI.

855

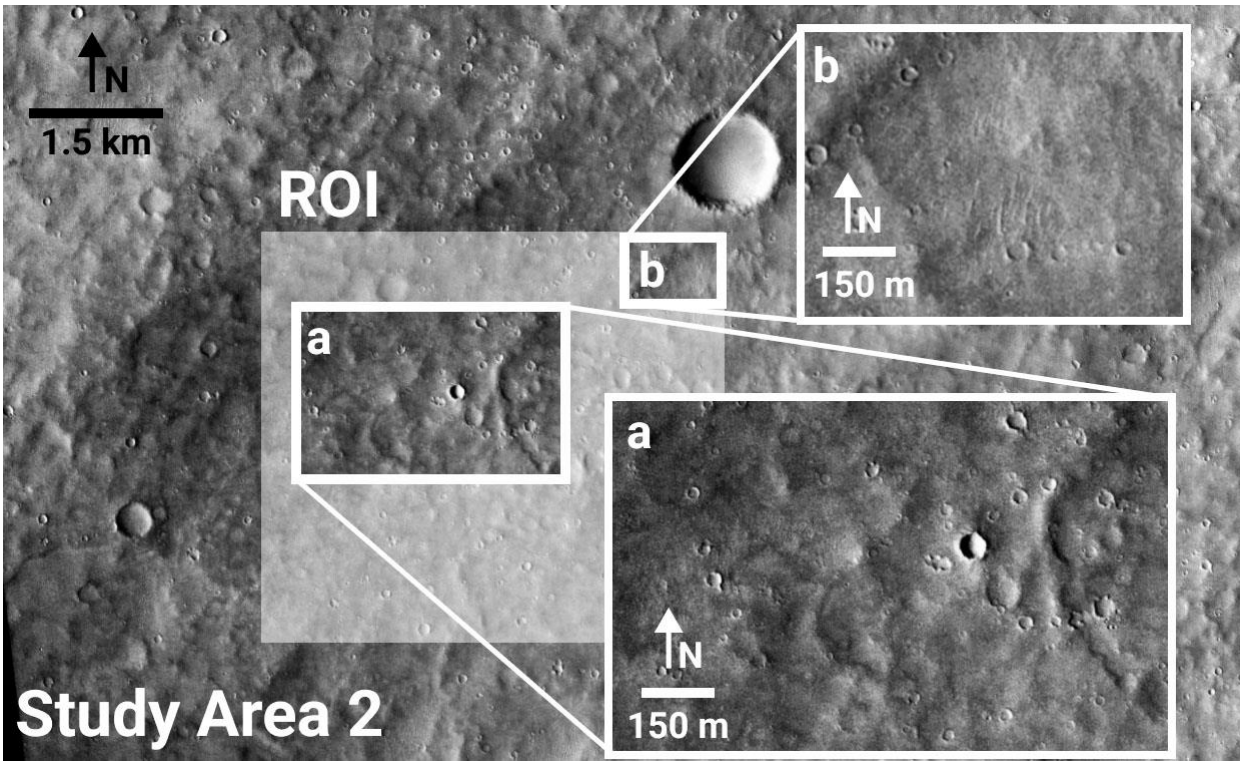

Figure 12. CTX image B05_011653_1714_XN_08S186W of study area 2 showing abundant small craters (a) and aeolian ripples (b).

856